Check for updates

JGR Space Physics

RESEARCH ARTICLE
10.1029/2020JA028068

Special Section:
Geospace Multi-Point Observations in Van Allen Probes and Arase Era

Plasma and Field Observations in the Magnetospheric Source Region of a Stable Auroral Red (SAR) Arc by the Arase Satellite on 28 March 2017

Yudai Inaba[1], Kazuo Shiokawa[1], Shin-ichiro Oyama[1,2,3], Yuichi Otsuka[1], Arto Oksanen[4], Atsuki Shinbori[1], Artem Yu Gololobov[5], Yoshizumi Miyoshi[1], Yoichi Kazama[6], Shiang-Yu Wang[6], Sunny W. Y. Tam[7], Tzu-Fang Chang[7], Bo-Jhou Wang[6], Shoichiro Yokota[8], Satoshi Kasahara[9], Kunihiro Keika[9], Tomoaki Hori[1], Ayako Matsuoka[10], Yoshiya Kasahara[11], Atsushi Kumamoto[12], Yasumasa Kasaba[12], Fuminori Tsuchiya[12], Masafumi Shoji[1], Iku Shinohara[10], and Claudia Stolle[13]

[1]Institute for Space-Earth Environmental Research, Nagoya University, Nagoya, Japan, [2]Ionosphere Research Unit, University of Oulu, Oulu, Finland, [3]National Institute of Polar Research, Tokyo, Japan, [4]Jyväskylän Sirius ry, Jyväskylä, Finland, [5]Institute of Physics and Technologies, North-Eastern Federal University, Yakutsk, Russia, [6]Academia Sinica Institute of Astronomy and Astrophysics, Taipei, Taiwan, [7]Institute of Space and Plasma Sciences, National Cheng Kung University, Tainan, Taiwan, [8]Department of Earth and Space Science, Graduate School of Science, Osaka University, Toyonaka, Japan, [9]Department of Earth and Planetary Science, School of Science, University of Tokyo, Tokyo, Japan, [10]Institute of Space and Astronautical Science, Japan Aerospace Exploration Agency, Kanagawa, Japan, [11]Graduate School of Natural Science and Technology, Kanazawa University, Kakuma-machi, Kanazawa, Japan, [12]Graduate School of Science, Tohoku University, Sendai, Japan, [13]Helmholtz Centre Potsdam, GFZ German Research Centre for Geosciences, Potsdam, Germany

Key Points:
- The conjugate measurements of a detached SAR arc on 28 March 2017 are analyzed using observations from the Arase satellite
- Swarm and GNSS-TEC data show that the electron density decreased and the electron temperature increased in the ionosphere above the SAR arc
- The observed plasmas and electromagnetic fields suggest that Coulomb collision is the most plausible mechanism for the SAR-arc generation

Supporting Information:
- Supporting Information S1

Correspondence to:
Y. Inaba,
inaba.yudai@isee.nagoya-u.ac.jp

Citation:
Inaba, Y., Shiokawa, K., Oyama, S.-i., Otsuka, Y., Oksanen, A., Shinbori, A., et al. (2020). Plasma and field observations in the magnetospheric source region of a stable auroral red (SAR) arc by the Arase satellite on 28 March 2017. *Journal of Geophysical Research: Space Physics*, *125*, e2020JA028068. https://doi.org/10.1029/2020JA028068

Received 2 APR 2020
Accepted 31 JUL 2020
Accepted article online 21 SEP 2020

©2020. American Geophysical Union. All Rights Reserved.

Abstract A stable auroral red (SAR) arc is an aurora with a dominant 630 nm emission at subauroral latitudes. SAR arcs have been considered to occur due to the spatial overlap between the plasmasphere and the ring-current ions. In the overlap region, plasmaspheric electrons are heated by ring-current ions or plasma waves, and their energy is then transferred down to the ionosphere where it causes oxygen red emission. However, there have been no study conducted so far that quantitatively examined plasma and electromagnetic fields in the magnetosphere associated with SAR arc. In this paper, we report the first quantitative evaluation of conjugate measurements of a SAR arc observed at 2204 UT on 28 March 2017 and investigate its source region using an all-sky imager at Nyrölä (magnetic latitude: 59.4°N), Finland, and the Arase satellite. The Arase observation shows that the SAR arc appeared in the overlap region between a plasmaspheric plume and the ring-current ions and that electromagnetic ion cyclotron waves and kinetic Alfven waves were not observed above the SAR arc. The SAR arc was located at the ionospheric trough minimum identified from a total electron content map obtained by the GNSS receiver network. The Swarm satellite flying in the ionosphere also passed the SAR arc at ~2320 UT and observed a decrease in electron density and an increase in electron temperature during the SAR-arc crossing. These observations suggest that the heating of plasmaspheric electrons via Coulomb collision with ring-current ions is the most plausible mechanism for the SAR-arc generation.

Plain Language Summary A stable auroral red (SAR) arc is an aurora with an optical red emission at latitudes slightly lower than the auroral zone. SAR arcs have been considered to occur due to the spatial overlap between the low-energy plasmaspheric electrons and the high-energy ring-current ions. In the overlap region, plasmaspheric electrons are heated by ring-current ions or plasma waves, and their energy is then transferred down to the upper atmosphere to cause the red emission. However, there have been no study conducted so far that quantitatively examined plasma and electromagnetic fields in the magnetospheric source region of SAR arcs. In this paper, we report the first quantitative evaluation of a SAR arc using an all-sky imager at Nyrölä, Finland, and the Arase satellite. The Arase observation shows that the SAR arc appeared in the overlap region between a plasmaspheric plume and the ring-current ions in the inner magnetosphere. The electromagnetic waves associated with the SAR arc were not observed. These observations suggest that the heating of plasmaspheric electrons by ring-current ions is the most plausible mechanism for the SAR-arc generation. This result provides

direct evidence of the previous theoretical expectation on the generation mechanism of red aurora at lower latitudes.

1. Introduction

A stable auroral red (SAR) arc is an aurora with a dominant 630.0 nm emission of oxygen atoms generated at subauroral latitudes. SAR arcs were first reported in southern France (Barbier, 1958) and have since been widely investigated. SAR arcs have been considered to be caused by electrons of several electronvolts (eV) that are generated in the overlap region between the plasmasphere and the ring-current ions (e.g., Kozyra & Nagy, 1997; Rees & Roble, 1975). Martinis et al. (2019) have observationally demonstrated that the SAR arc is geomagnetically conjugate phenomena between Northern and Southern Hemispheres. In addition to these optical features, various other features of SAR arcs have been reported. For example, Roach and Roach (1963) reported that the average height of the peak intensity of the 630.0 nm emission was 400 km. Marovich (1966) found that SAR arcs were observed in ~20% of nighttime observations during a solar maximum. Foster et al. (1994) conducted simultaneous observations of a SAR arc with a Defense Meteorological Satellite Program (DMSP) satellite, an all-sky camera, and the Millstone Hill radar. They found that the ionospheric trough and the subauroral ion drift occurred simultaneously in the SAR arc region. Shiokawa et al. (2013) observed a SAR arc event that occurred in the initial phase of a geomagnetic storm and showed that the plasmasphere and ring-current ions overlapped spatially due to the inward development of the ring current caused by storm-time substorms. Mendillo et al. (2016) reported that a SAR arc could develop zonally from east to west and additionally observed a patchy 557.7 nm emission (oxygen atom). Shiokawa et al. (2009, 2017) and Takagi et al. (2018) used all-sky imagers installed at subauroral latitudes and observed the detachment of SAR arcs from the auroral oval to lower latitudes associated with substorm recovery. Takagi et al. (2018) showed that these detachments occur mainly in the premidnight sector. They explained that westward-drifting ions injected from the night side caused a higher occurrence of these detachments in the premidnight sector. Recently, Chu et al. (2019) reported the simultaneous observation of a STEVE aurora collocated with a SAR arc using ground-based instruments and Van Allen Probes-B. They mainly focused on the STEVE and concluded that the generation mechanism is different between SAR arc and the STEVE. However, to the best of our knowledge, there has been no study conducted so far that quantitatively examined plasma and electromagnetic fields in the inner magnetosphere associated with SAR arcs.

It has been considered that the energy of the precipitating electrons (or heat flux) that are the source of SAR-arc emission is several eV. Kozyra and Nagy (1997) argued that there are three possible mechanisms to generate these low-energy electrons. The first hypothesis is the Coulomb collision between plasmaspheric electrons (energies less than 1 eV) and ring-current ions (several tens of keV); the energy is transported into the ionosphere via heat conduction or as a low-energy electron flux (e.g., Cole, 1965; Prolss, 2006). The second hypothesis is that the Landau damping of electromagnetic ion cyclotron (EMIC) waves causes heated electrons and their pitch angle scattering and thereby causes these electrons to precipitate into the ionosphere (Cornwall et al., 1971). Wang et al. (2019) recently showed the possibility of heating plasmaspheric electrons by Landau damping of EMIC waves using a test-particle simulation. The third hypothesis is that the kinetic Alfven waves (KAWs) whose electric field is parallel to the magnetic field accelerate plasmaspheric electrons to the ionosphere. Lanzerotti et al. (1978) reported the observation of KAWs via ground-based measurements in a conjugate region of a SAR arc. Kozyra et al. (1987) argued that the energy transfer to the background electron is maximized for ring-current protons with energies of 1–2 keV and for ring current oxygen ions with energies of tens of keV. Furthermore, they noted that oxygen ions are the major source of electron heating. However, which mechanism is the dominant source of electron heating remains unknown because no quantitative evaluation have been made for the high-altitude energy source of a SAR arc.

In this study, we report first quantitative evaluation of the conjunction event of a SAR arc using an all-sky cooled-CCD imager at Nyrölä, Finland, and the Arase satellite in the magnetosphere in the Southern Hemisphere at a magnetic latitude of −33° at L ~3.7. Additionally, simultaneous and co-located observations from the Swarm satellites and ground-based total electron content (TEC) maps are used to support the analysis. These observations enable us to discuss the validity of the three possible mechanisms for the generation of precipitating electrons. EMIC waves and KAWs were not observed by Arase. The SAR arc was mapped to

the overlap region between the ring-current ions and the plasmasphere identified by the Arase satellite. We conclude that the heating of plasmaspheric electrons via Coulomb collision with ring-current ions is the most plausible mechanism for the generation of the SAR arc.

2. Instrumentation

The all-sky cooled-CCD imager (imager #18) that was used in the present analysis is part of the Optical Mesosphere Thermosphere Imagers (Shiokawa et al., 1999, 2000) and is installed at Nyrölä, Finland (62.34°N, 25.51°E, magnetic latitude [MLAT]: 59.44°N, L = 3.87) at subauroral latitudes by the PWING project (Shiokawa et al., 2017) to capture faint auroral and airglow emission. The imager was equipped with five optical filters with a narrow passband (transmission width: 1.5–2.0 nm) that transmit the emission of specific lines of aurora and night airglow. The filters are for emissions at wavelengths of 557.7 nm (oxygen atoms), 630.0 nm (oxygen atoms), 700–1,000 nm (OH-band), 486.1 nm (hydrogen atoms), and 572.5 nm (background continuous emission). In this analysis, 557.7 and 630.0 nm images were used to observe the aurora and airglow. The all-sky imager used in this study was calibrated to derive the absolute intensity using optical facilities at the National Institute of Polar Research, Japan (Shiokawa et al., 2000). Typical read-out noise of the CCD camera is less than a few Rayleigh (corresponding to ~10 counts).

The exploration of energization and radiation in geospace (ERG, also called Arase) satellite (Miyoshi, Shinohara, et al., 2018) was launched on 20 December 2016 and started regular observations on 23 March 2017. Arase has been flying in an elliptical earth orbit of 400 × 32,000 km with an orbital period of about 570 min. This study used instruments onboard the Arase satellite, namely, the Plasma Wave Experiment (PWE) (Kasahara et al., 2018), the Electric Field Detector (EFD) (Kasaba et al., 2017), the High-Frequency Analyzer (HFA) (Kumamoto et al., 2018), the Magnetic Field Experiment (MGF) (Matsuoka et al., 2018), the Low-Energy Particle Experiments–Electron Analyzer (LEP-e) (Kazama et al., 2017), and the Medium-Energy Particle Experiments–Ion Mass Analyzer (MEP-i) (Yokota, 2017). The Arase satellite data were analyzed using the Space Physics Environment Data Analysis Software (SPEDAS) tool (Angelopoulos et al., 2019).

This study also used two-dimensional TEC data with a temporal and spatial resolution of 5 min and 0.5° × 0.5°, respectively, which were derived from Global Navigation Satellite System (GNSS) data in Receiver INdependent EXchange (RINEX) format. The global GNSS data were obtained in January 2020 from more than 9,000 GNSS stations installed all over the world. The absolute values of vertical TEC were estimated using the technique developed by Otsuka et al. (2002). Slant TEC values were converted into vertical TEC values near the geographic longitude of the Nyrölä station under the assumption that the ionosphere is a thin layer at a height of 400 km. The slant TEC data with a zenith angle of less than 75° were selected, and a keogram (geographic latitude–time plot) of TEC was created.

Swarm is a constellation mission consisting of three identical satellites launched by the European Space Agency (ESA) on 22 November 2013 (e.g., Olsen et al., 2016). In addition to data from the Arase satellite, this study used data from two of the three Swarm satellites, namely, Swarm-Alpha (Swarm-A) and Swarm-Charlie (Swarm-C). These two satellites fly almost side-by-side in polar orbits at an initial altitude of 480 km with a separation of 1.4° in longitude at the equator and at an inclination angle of 87.35°. Each Swarm satellite is equipped with an absolute scalar magnetometer and a fluxgate vector field magnetometer including star trackers to obtain high-precision absolute magnetic field vectors. The time and position of the satellites are provided by onboard GPS receivers. Swarm observes electron density and electron temperature, using I-V characteristics of the electric potential offset of the satellite measured by the Langmuir probes (Knudsen et al., 2017). Lomidze et al. (2018) calibrated and validated the measurements of plasma density and temperature using ground-based radars and satellite radio occultation measurements.

3. Observation Results

Figure 1 shows the AU, AL, and SYM-H indices (Iyemori, 1990; Iyemori & Rao, 1996) for the interval during the SAR arc event which was studied in this work. In the present analysis, the SAR arc was detached (separated equatorward and became distinct from the diffuse aurora in the main auroral oval) at ~1840 UT, shown as the left vertical dashed line in Figure 1. The 4-day SYM-H variation (Figure 1b) indicates that the SAR arc occurred during the recovery phase of the geomagnetic storm that began on 27 March 2017. As shown in

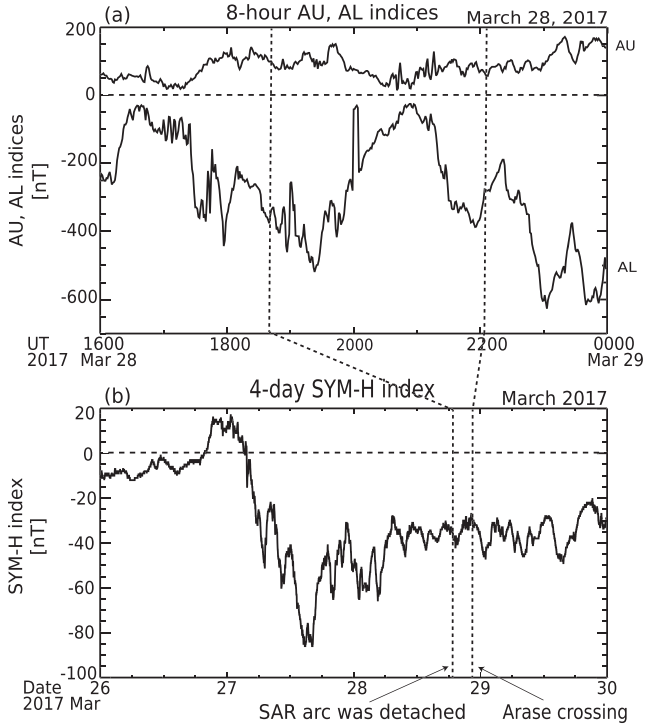

Figure 1. (a) Eight-hour AU and AL indices on 28 March 2017. (b) Four-day SYM-H index on 26–30 March 2017. The left vertical dashed line shows the time when the SAR arc was detached and the right vertical dashed line shows the time when Arase crossed the SAR arc.

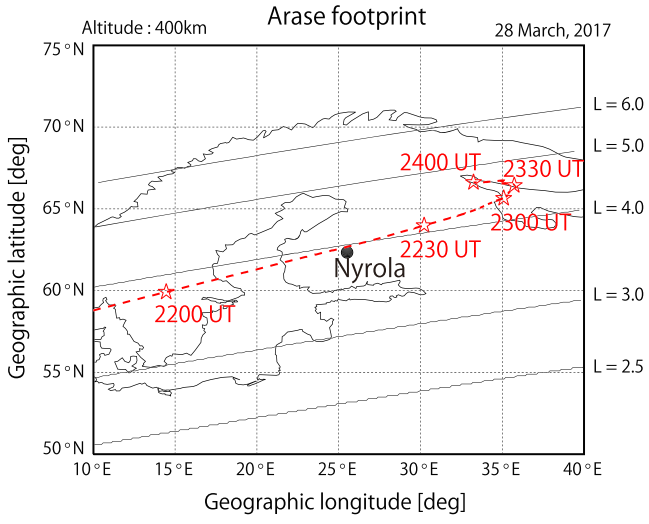

Figure 2. Trajectory of the ionospheric footprint of the Arase satellite mapped at an altitude of 400 km using the TS05 model.

Figure 1a, several substorms occurred in association with negative excursions of the AL index (World Data Center for Geomagnetism, Kyoto et al., 2015). The SAR arc analyzed in this study was detached around the end of the expansion phase of the substorm that started at ~1640 UT, as shown later in Figure 4a. Here, we defined the start of the expansion phase using the AU/AL indices.

Figure 2 shows the trajectory of the ionospheric footprint of the Arase satellite mapped to an altitude of 400 km using the Tsyganenko-Sitnov 2005 (TS05) magnetic field model (Tsyganenko & Sitnov, 2005) when the satellite crossed the SAR arc on 28 March 2017. To drive TS05 model, the solar wind parameters and W-parameters in TS05 web repository published by N. Tsyganenko were used. The black point indicates the location of Nyrölä, Finland, where the ground all-sky imager was operated. The five oblique lines indicate positions of L = 2.5, 3.0, 4.0, 5.0, and 6.0 from the low latitude side, respectively. Here, L is the L-shell derived from the International Geomagnetic Reference Field model (Thébault et al., 2015). Arase's ionospheric footprint passed over Nyrölä from the southwest to the northeast from 22:00 to 23:00 UT.

Figure 3 shows auroral images taken at 1914:50–2240:20 UT on 28 March 2017 at Nyrölä through the 630.0 nm filter. These images were converted to geographical coordinates by assuming an emission altitude of 400 km. The SAR arc is in the south-center of the images and appears as an east-west elongated emission structure.

The northern halves of the images in Figure 3 are saturated, indicating the existence of the main auroral oval. The SAR arc extended in the east-west direction at around 62° latitude from 1840 UT (before the time shown in Figure 3), slightly to the south of the diffuse aurora in the auroral oval in the images. After 1840 UT, the SAR arc developed equatorward down to ~60° latitude. After this time, the north-south boundaries of the SAR arc became blurred, and the arc's latitudinal width increased. This SAR arc existed from 1840 to 2330 UT. Mendillo et al. (2013) showed that the average location of SAR arc and the average equatorward edge of diffuse aurora are barely separated statistically, which indicates that our SAR-arc definition is valid. The footprint of the Arase satellite clearly crossed the SAR arc at around 2201–2206 UT.

Figure 4a shows a keogram of TEC at the geographic longitude of the Nyrölä station. A clear TEC depletion (<3.0 TECU) with a latitudinally narrow structure can be observed below 66° latitude, with the latitude of this depletion decreasing with time. This depletion corresponds to the ionospheric trough. The white curve in Figure 4a indicates the location of the trough minimum.

Figures 4b and 4c show keograms for 630.0 and 557.7 nm images that are converted to geographical coordinates by assuming an emission altitude of 400 and 120 km, respectively. These keograms contain information on the temporal variation of emission intensity only at the longitude of Nyrölä. Figure 4b shows that the SAR arc was detached from the southward boundary of the main oval (~64°N) just after 1840 UT, and this detached SAR arc lasted for more than 5 hr until about 2400 UT. Because the SAR arc peeled away from east to west, it was detached earlier than 1840 UT to the east of Nyrölä and later than 1840 UT to the west of Nyrölä. On the other hand, such a structure detached from the main oval is not found in the 557.7 nm keogram shown in Figure 4c, indicating that

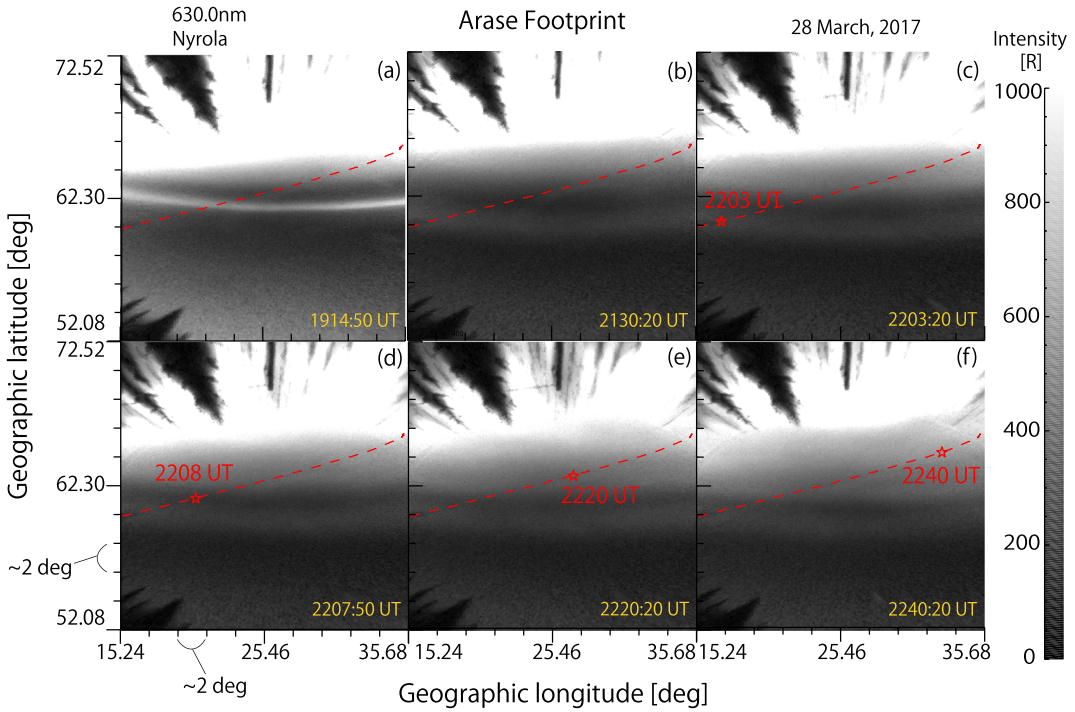

Figure 3. 630 nm images captured with an all-sky airglow imager at Nyrölä on 28 March 2017 at the following times (all in UT): (a) 1914:50, (b) 2130:20, (c) 2203:20, (d) 2207:50, (e) 2220:20, and (f) 2240:20. These images were converted to geographic coordinates by assuming an auroral emission altitude of 400 km. Red dashed curves show the trajectory of the footprint of the Arase satellite mapped at an altitude of 400 km using the TS05 model. The red star shows the position of the footprint of Arase at the time when the image was taken. The horizontal and vertical axes correspond to the geographic latitude and geographic longitude (20.48° × 20.48° centered on Nyrölä), respectively. The grayscale represents the 630.0 nm emission intensity. The black shadows in the upper left and lower left are trees in the surrounding forest.

the observed 630 nm arc structure is a SAR arc. In Figure 4b, the location of the ionospheric trough minimum almost coincides with the location of the SAR arc over the time during which it occurs. However, the newly detached, bright SAR arc at about 1840–1925 UT appears at a slightly higher latitude than the trough minimum. The 630.0 nm intensity exceeded 500 R during this period and subsequently decreased to ~200–300 R.

Continuous 630 nm images are also shown in Movie S1. From this movie, it can be seen that the SAR arc was detached from the diffuse aurora in the auroral oval and remained stable for a long time, and additionally that the SAR arc experienced a westward motion at about 1840–2000 UT.

The Swarm-A and -C satellites also crossed the SAR arc at an altitude of ~450 km. Figure 5a shows the orbit of the Swarm-A and -C satellites at ~2320 UT on 28 March 2017. Swarm-A and -C crossed the SAR arc at around 2320:10 UT. Figure 5 also shows the electron density (b), electron temperature (c), and field-aligned currents (d) as measured by the Swarm-A (red) and -C (blue) satellites, as well as timestamps marked every 50 s from 2318:30 to 2322:50 UT (e) and the 630.0 nm airglow/auroral intensity at the Swarm-A (red) and -C (blue) location observed by the camera at Nyrölä (f). As shown in Figure 5a, Swarm-C also crossed the SAR arc almost simultaneously. Although the variation of the emission intensity shown in Figure 5f was obtained from pixels along the Swarm trajectories for every 1 s, the temporal resolution of the camera was 90 s. Additionally, it should be noted that the emission intensities at multiple positions were obtained from a single image. In other words, Figure 5f includes temporal and spatial variations of the 630.0 nm emission. As shown in Movie S1, the SAR arc had only minor spatial and temporal variations.

In Figure 5a, we can identify the time when the Swarm-A and -C satellites crossed the SAR arc by the trajectory of the Swarm satellites. As can be seen in Movie S1 and Figure 5a, the east-west weak emission indicated by the pink arrow is the SAR arc immediately before its disappearance. In Figure 5f, a shoulder-like

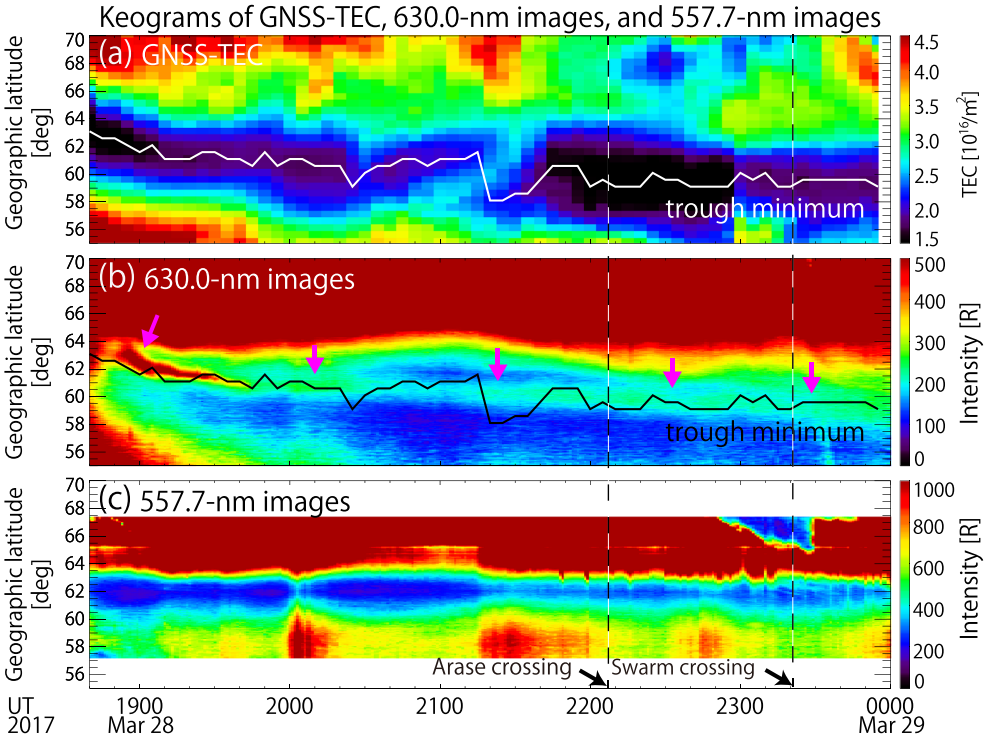

Figure 4. (a) Keogram of the total electron content (TEC) map at the longitude of Nyrölä, and keograms obtained by slicing the (b) 630.0 nm and (c) 557.7 nm images at Nyrölä from 1840:00 UT to 2400:00 UT on 28 March 2017. The white curve in (a) and the black curve in (b) indicate the location of the trough minimum. Pink arrows in (b) indicate the location of the SAR arc. The left and right vertical black dashed lines represent the timing when the Arase satellite and the Swarm satellite crossed the SAR arc, respectively.

enhancement of 630 nm intensity is seen at the timing of the SAR arc crossing. The emission from the auroral oval overhangs the lower latitudes, so that clear intensity peak at 630.0 nm is not visible in Figure 5f at the timing of SAR arc crossing. There is a remarkable peak at 53 degrees in geographic latitude in Figure 5f. This localized emission appears only in the images at around ~2317 UT for less than 10 min. It is a localized cloud.

As can be seen in Figure 5d, the field-aligned current was not observed at the location of the SAR arc by either of the Swarm-A and -C satellites. In Figure 5b, the electron density decreases from 51° to 61° latitude and nearly reaches its minimum at the location of the SAR arc. This low-electron density corresponds to the ionospheric trough shown in the TEC keogram in Figure 4a. In Figure 5c, the electron temperature increases from 53° to 60° latitude and has a peak at the location of the SAR arc, which is also consistent with the signature of the ionospheric trough (e.g., Foster et al., 1994). It is noteworthy that the electron density slightly increases at the location of the SAR arc (Figure 5b); this may indicate moderate supply (precipitation) of electrons heated by Coulomb collisions from the magnetosphere to the SAR arc.

Figure 6 shows data from the Arase satellite during its crossing of the SAR arc. During the time interval shown in this figure, Arase was moving outward from L ~2.2 to L ~4.1 in the Southern Hemisphere at MLATs of approximately −33° to approximately −31°, where L is McIlwain's L-parameter (McIlwain, 1961). The figure shows the electric field spectra obtained by PWE/HFA (a), the MEP-i proton flux (b), the LEP-e electron flux (c), the electric field in solar magnetospheric (SM) coordinates measured with the EFD (d), the satellite potential from the EFD (e), and the emission intensity of 630.0 nm at the footprint of Arase at an altitude of 400 km at Nyrölä (f). Again, it should be noted that the variation of the emission intensity in Figure 6f was obtained from pixels along Arase's orbit for every 6 s, while the temporal resolution of the camera was 90 s. It should also be noted that the emission intensities at multiple positions were obtained from a single image.

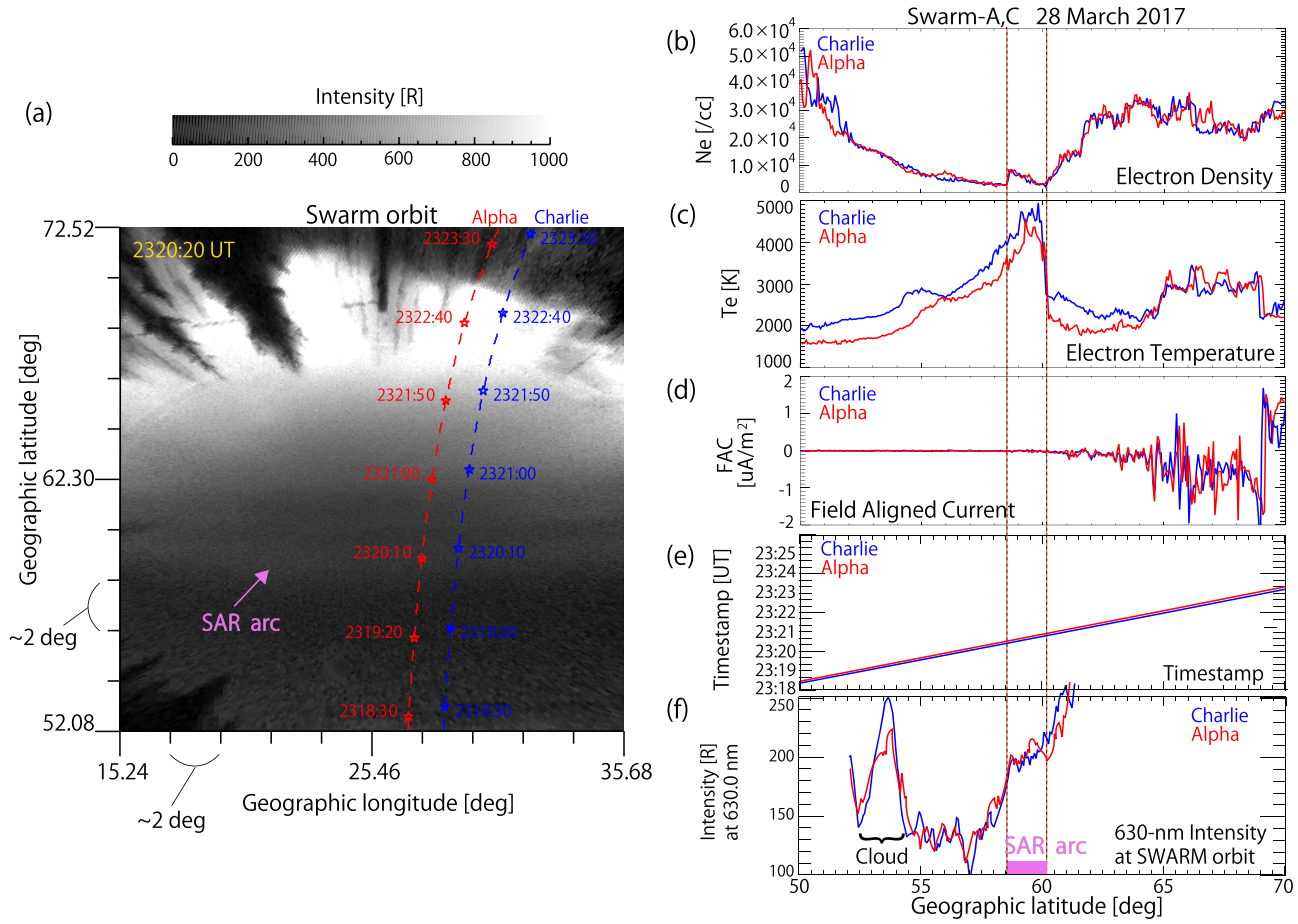

Figure 5. (a) 630 nm image captured with an all-sky airglow imager at Nyrölä at 2320:20 UT on 28 March 2017. This image was converted to geographic coordinates by assuming an auroral emission altitude of 400 km. Red and blue dashed curves show the trajectories of the Swarm-A and -C satellites, respectively. (b) Electron density, (c) electron temperature, and (d) field-aligned current measured by the Swarm-A (red) and -C (blue) satellites. (e) Timestamps marked every 50 s from 2318:30 to 2322:50 UT, and (f) 630.0 nm airglow/auroral intensity observed at Nyrölä at the locations of the Swarm-A (red) and -C (blue) satellites. The two black vertical dashed lines in (b)–(f) indicate the width of the SAR arc taken from panel (f) for the Swarm-A satellite.

In this analysis, the TS05 model was used to map the Arase satellite from the magnetosphere to the ionosphere. In order to verify the ambiguity of the field-line mapping, we compared the magnetic field of the TS05 model at the location of the Arase satellite with the magnetic field observed by the Arase satellite at the peak location of the SAR arc. The difference in the magnetic field ($\boldsymbol{B_{satellite} - B_{model}}$) was (20.384, 0.110, and 28.435) nT in geocentric solar magnetospheric (GSM) coordinates. We searched for a position where ($\boldsymbol{B_{satellite} - B_{model\_shifted}}$) becomes close to zero by changing the position of Arase in the model. We obtained the position $\boldsymbol{\Delta R}$ where $\boldsymbol{B_{satellite} - B_{model\_shifted}}$ becomes (0.066, 0.179, and −0.102) nT is $\boldsymbol{\Delta R}$ = (−0.0092, +0.00564, and +0.0189) Re in GSM coordinates from the original position, indicating the ambiguity of the position of Arase. The intensity change at the moved position of Arase is shown by the red dashed line in Figure 6f, and the peak time is almost unchanged. Although not shown in the figure, the SAR arc peak is almost the same even when the Tsyganenko 01 model was used (Tsyganenko, 2002a, 2002b).

In order to evaluate the ambiguity arising from the altitude of the SAR-arc emission, the mapping altitude was changed from 400 to 300 km. The 630 nm emission at the footprint (300 km) is shown by a blue dashed line in Figure 6f. The SAR arc peak did not change in this case either, because the SAR arc was observed near the zenith of Nyrölä. Based on these analyses, we consider that the location of the SAR arc peak is accurate enough within the range of the dashed and solid curves in Figure 6f.

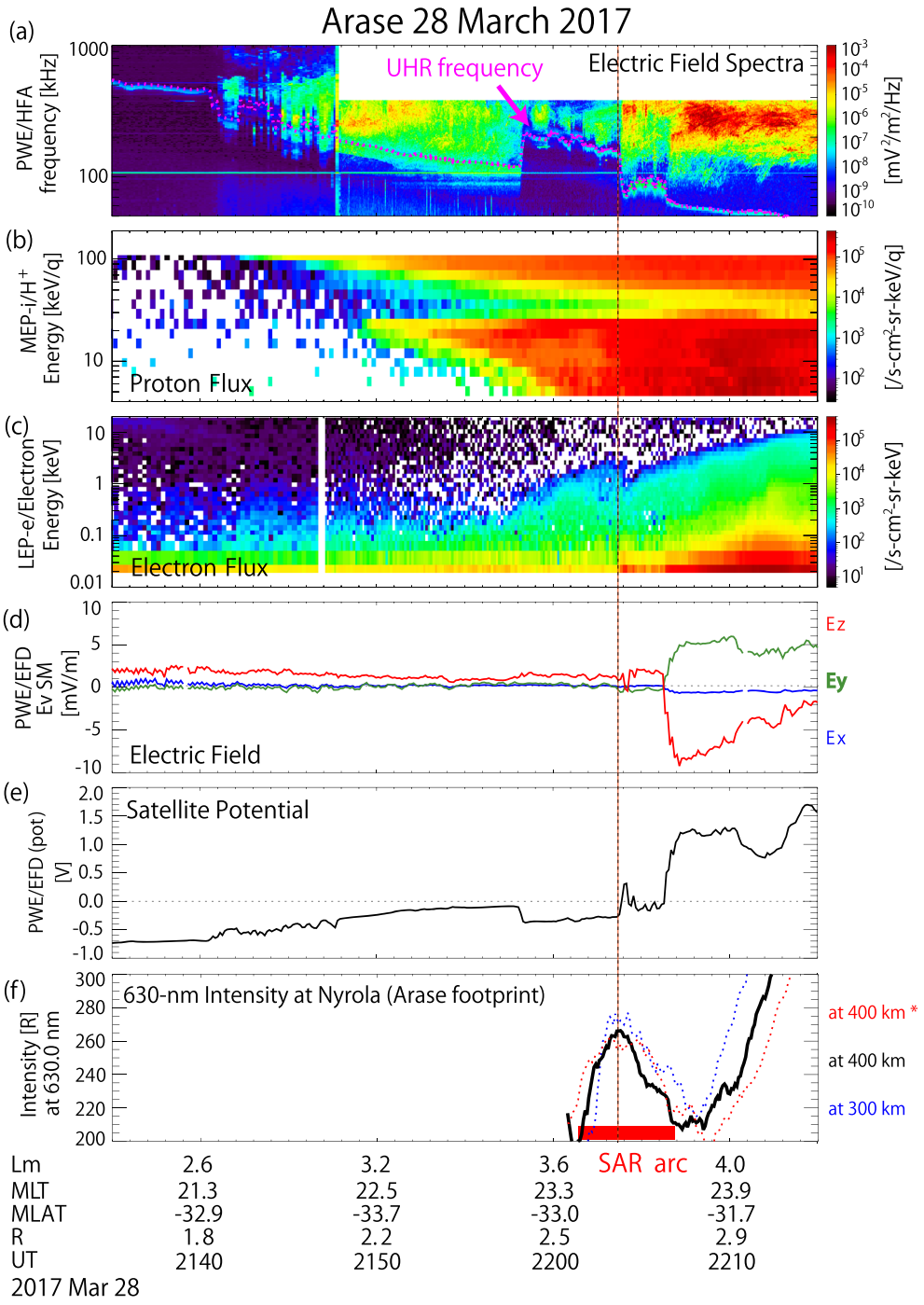

Figure 6. (a) Electric field spectra obtained by PWE/HFA, (b) MEP-i medium-energy proton flux, (c) LEP-e low-energy electron flux, (d) electric field in SM coordinates measured by EFD, (e) satellite potential measured by EFD, and (f) 630.0 nm intensity at the Arase footprint at an altitude of 400 km observed at Nyrölä. The horizontal axis spans 2135 to 2215 UT. The position of the Arase satellite is also shown on the horizontal axis as geomagnetic parameters. Note that MLAT does not represent the magnetic latitude of the ionospheric footprint, but the latitudinal angle at which the satellite is located from the magnetic equatorial plane to the Earth's center. The vertical black dashed line shows the timing of the maximum intensity of the SAR-arc emission. The pink dotted curve shows the UHR frequency. The intensity change at the moved position of Arase is shown by the red dashed line in Figure 6f.

As can be seen in the high-frequency electric field spectra from the PWE/HFA instrument (pink dotted curve in Figure 6a), the upper hybrid resonance (UHR) frequency dropped substantially at ~2140, indicating that Arase exited the plasmasphere at this time. Subsequently, the UHR frequency rose again at ~2158 UT, suggesting that Arase entered a plasma plume. The outer boundary of this plume was located exactly at the intensity peak of the SAR arc.

The proton flux with energies of 5–100 keV/q of MEP-i shown in Figure 6b suggests that Arase observed the ring-current ions when it crossed the SAR arc. In Figure 6b, an energy-L dispersion (nose structure) can be observed at ~2150–2200 UT. Such structures are often observed in ring-current ions (e.g., Ejiri, 1978; Smith & Hoffman, 1974; Vallat et al., 2007). In Figure 6c, the electron flux below 50 eV slightly increases around the peak of the SAR arc. At ~2204:10 UT, the satellite potential in Figure 6e and the electric field in the Z_{SM} component in Figure 6d show positive and negative excursions, respectively, with a duration of 20–30 s. The satellite potential is related to the ambient electron density and the electron temperature (e.g., Anderson et al., 1994). The Arase satellite was positively charged at ~2204:10 UT possibly due to the electron density gradient at the outer boundary of the plume. This satellite potential enhancement may have caused acceleration of electrons toward the satellite, and thus, the increase of low-energy electron fluxes below 50 eV in Figure 6c. Therefore, these enhancements of satellite potential and low-energy electron flux may not be related to the SAR arc generation. A small negative excursion of the electric field (~2 mV/m) in the Z_{SM} direction coincided with the satellite potential enhancement at ~2204:10 UT. However, the negative excursion does not correspond to the entire width of the SAR arc. This indicates that Arase did not observe a SAR-arc associated converging electric field (and corresponding flow shear), which is often observed in regular auroral arcs in the auroral oval (e.g., Burke et al., 1982; Coroniti & Pritchett, 2014; Shiokawa et al., 1996).

Figure 7 shows (a) electron density calculated from the UHR frequency, (b) omnidirectional oxygen ion flux, (c) omnidirectional proton flux, and (d) magnetic field deviation from 5 min running averages in SM coordinates, all observed by the Arase satellite, as well as 630.0 nm airglow/auroral intensity observed at the Arase footprint at a height of 400 km (e).

As seen in the electron density in Figure 7a, Arase exited the plasmasphere at ~2140 UT, entered the plasma plume at 2158 UT, and exited the plasma plume at 2204 UT when it crossed the SAR arc. The observed density variations seen at 2142–2148 UT may correspond to density irregularities often found outside the plasmapause (e.g., Horwitz et al., 1986). The plasma plume was embedded in the region where the ring-current ions had a nose structure. As shown in Figure 7c, the oxygen ion flux intensified at 2205–2210 UT at energies of ~8–20 keV/q during the crossing of the SAR arc. In Figure 7d, there is no magnetic field fluctuation associated with the crossing of the SAR-arc on the scale of several nT, suggesting that there is no magnetic waves with a meaningful amplitude associated with the SAR arc.

Figures 8a–8c show dynamic spectra of the magnetic field observed by Arase at frequencies of 0.3–10 Hz in order to investigate the possibility that the Landau damping of EMIC waves heats plasmaspheric electrons. As can be seen from the spectra, the power spectral density (PSD) shown in Figure 8 are mostly less than 10^{-2} nT^2/Hz, and no clear enhancement of EMIC waves is identified above the SAR arc as compared with the non-SAR arc region. The PSD increases at both ends of the SAR arc, in addition to a weak enhancement at the peak of the arc. This increase in PSD corresponds to the location of the density gradient in Figure 7a. These PSD enhancements may be related to the fact that radial density gradients can guide EMIC waves and favor wave growth conditions (e.g., Chen et al., 2009; de Soria-Santacruz et al., 2013). However, these PSD enhancements are weak as discussed in section 4 and do not correspond to the structure of the SAR arc.

In order to evaluate the magnetic field variation at lower frequencies, we analyzed the 8 s data of Arase/MGF. Figures 8d–8f indicate dynamic wavelet spectra of the magnetic field observed by Arase at a frequency range of 1–62.5 mHz. As seen in these panels, local enhancement of PSDs associated with the SAR arc was not observed. The PSDs at ~10 mHz over the SAR arc were at most ~5 nT^2/Hz which is too weak to generate SAR arc as discussed in section 4.

4. Discussion

Figures 1a and 1b show that the SAR arc was observed during the recovery phase of the geomagnetic storm and during the occurrence of recurrent substorms. This is consistent with past observations of SAR arcs (e.g.,

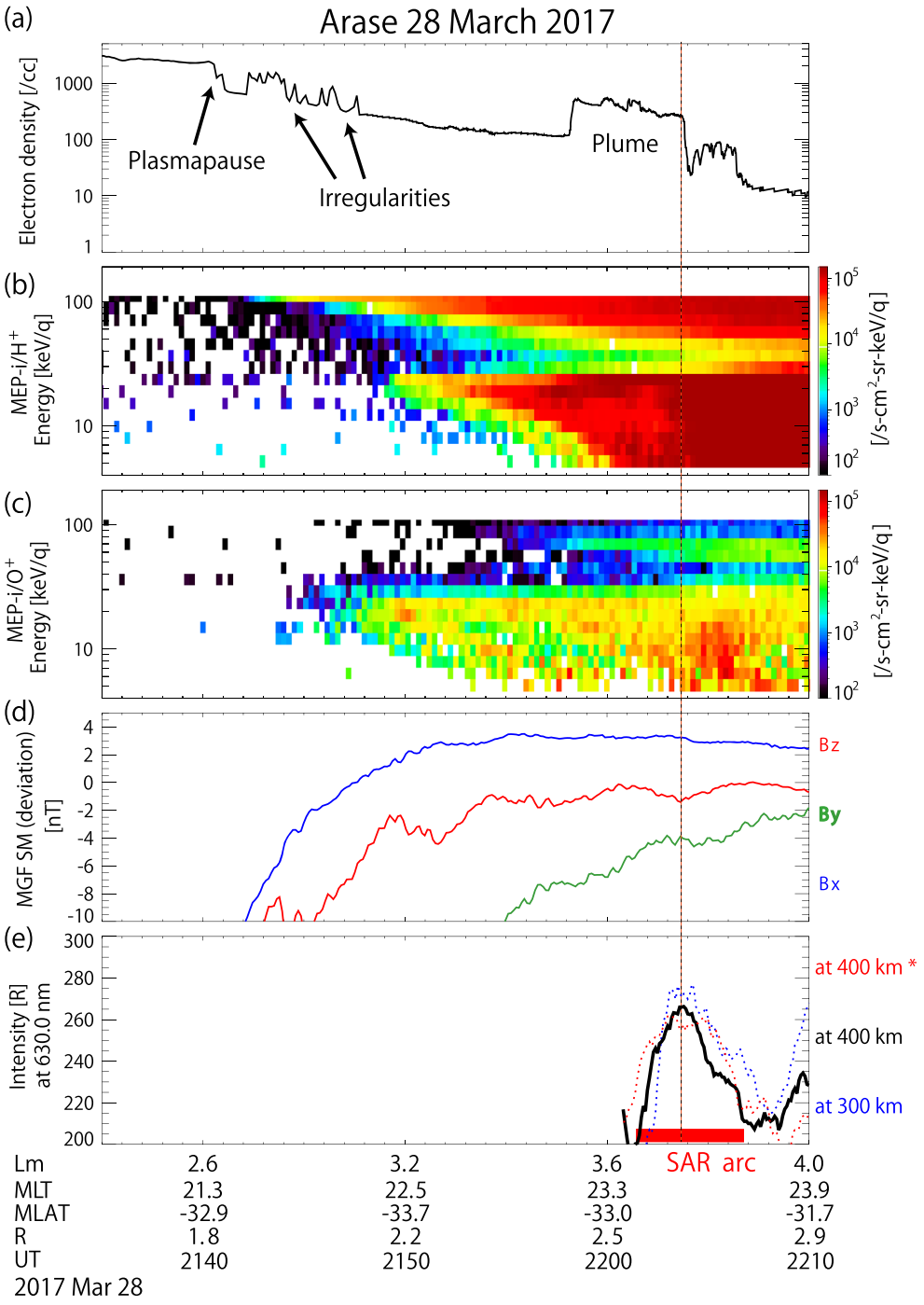

Figure 7. (a) Electron density calculated from the UHR frequency, (b) omnidirectional oxygen ion flux, (c) omnidirectional proton flux, (d) magnetic field deviation from 5 min running averages, all observed by the Arase satellite, and (e) 630.0 nm airglow/auroral intensity observed at Nyrölä at the Arase footprint. The horizontal axis is from 2135 to 2210 UT. The vertical dashed line indicates the time of peak intensity of the SAR-arc emission at the footprint. Figures 7b and 7e are based on the same data as those in Figures 6b and 6f, respectively.

Kozyra et al., 1987; Mendillo et al., 2016; Rees & Roble, 1975). Additionally, Figure 1a shows that the SAR arc was detached from the diffuse aurora in the auroral oval around the end of the expansion phase of a substorm. This is also consistent with the characteristics of SAR-arc detachment reported by Takagi et al. (2018).

Chu et al. (2019) showed a conjunction event of a STEVE aurora collocated with a SAR arc using all-sky imagers and Van Allen Probe-B. They focused on the STEVE generation mechanism and concluded that the

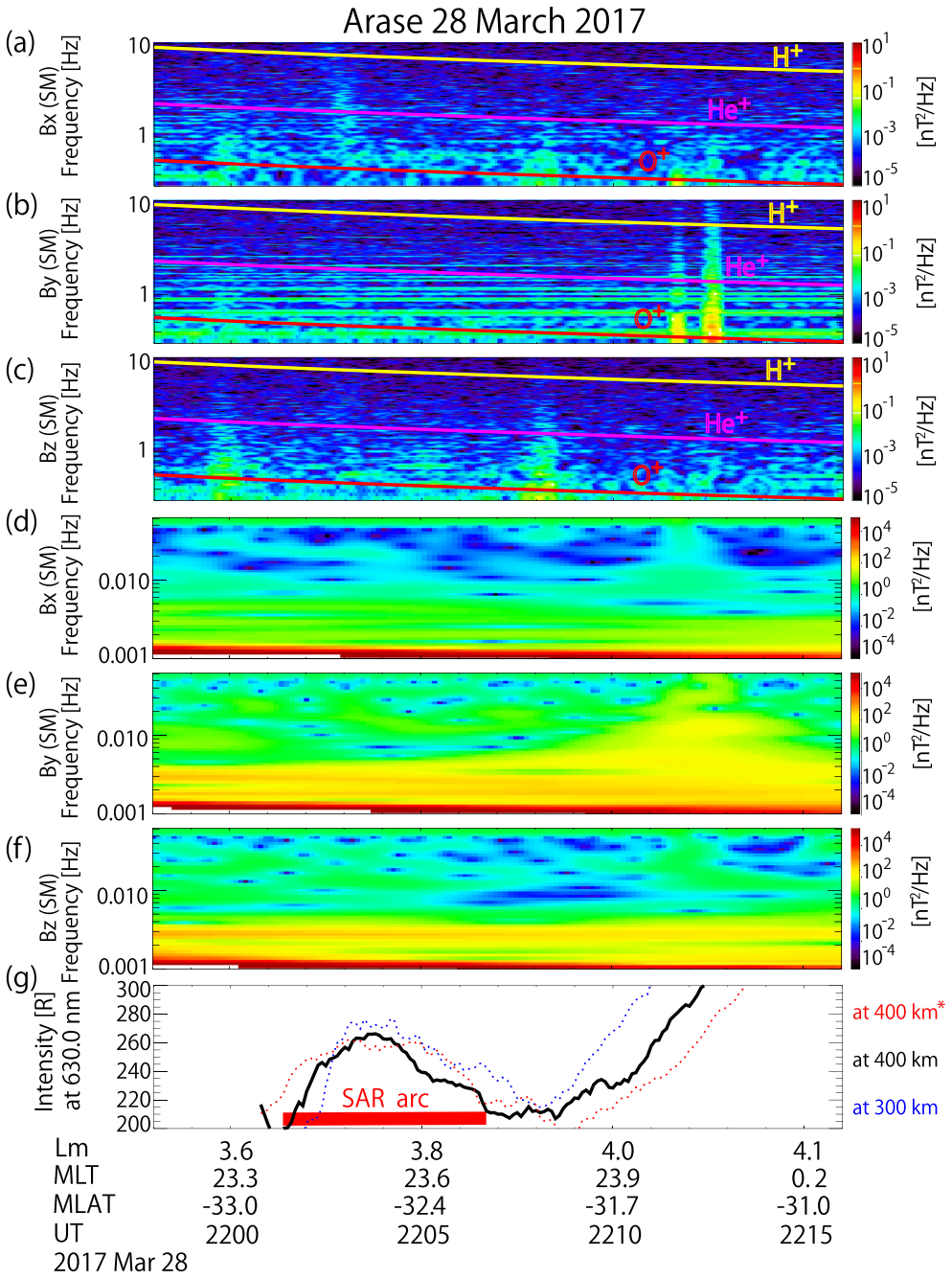

Figure 8. (a–c) Fast Fourier transform spectra of the magnetic field at a frequency range of 0.3–10 Hz. (d–f) Wavelet spectra of the magnetic field at a frequency range of 1–62.5 mHz observed by the MGF onboard the Arase satellite. (g) 630.0 nm airglow/auroral intensity observed at Arase's ionospheric footprint. Panel (g) is based on the same data as Figures 6f and 7e. The yellow, pink, and red curves in (a–c) represent the gyro frequencies at the magnetic equator of protons, helium, and oxygen, respectively.

SAR arc was originated by Coulomb collision between plasmaspheric cold electrons, ions, and ring current ions, based on the observed overlap of the plasmasphere and the ring current ions above the SAR arc. However, they did not evaluate quantitatively on the Coulomb collision processes and did not investigate electromagnetic waves that are another possible mechanism of the SAR arc generation.

Kozyra and Nagy (1997) introduced three mechanisms—namely, Coulomb collision, EMIC waves, and KAWs—by which the plasmaspheric electrons are heated by the ring-current ions. EMIC waves and

KAWs are both generated at the magnetic equator. Coulomb collisions occur more effectively as ring-current ions approach the earth along the magnetic field lines, because the plasmaspheric electron density increases at lower altitudes. Based on the present observations, these hypotheses are verified in the following sections.

4.1. Coulomb Collisions as a Source of SAR Arc Energy

Previous studies have suggested that the plasmaspheric electrons are heated by the ring-current ions via Coulomb collision and the consequent heat flux transported to the ionosphere causes SAR arcs. In the present observations, the plasmasphere and the ring-current ions were actually found to overlap. However, as shown in Figure 7, the overlap region was wider than the width of the SAR arc observed by the all-sky imager. We consider two possible causes for the difference in the widths of the overlap region and the SAR arc. One is that the oxygen ion flux at ~8–20 keV/q, which is locally intensified near the SAR arc (Figure 7c), could be important for the generation of the SAR arc. Kozyra et al. (1987) claimed that oxygen ions at energies of several tens of keV contribute significantly to the generation of SAR arcs. Another possible cause is that the ring-current ions below ~5 keV/q, which were not measured by Arase, contributed to the Coulomb collision. The width of the overlap region between ring-current ions at ~5 keV/q and the plasma plume is comparable with that of the SAR arc due to the energy-L dispersion of the nose structure, as shown in Figures 7b and 7a. According to Kozyra et al. (1987), protons with energies of 1–2 keV cause Coulomb collisions most efficiently.

We further examined the former possible cause of the difference in the widths of the overlap region and the SAR arc, namely, the local enhancement of oxygen ions. Figure 9 shows the calculated heat flux from (a) protons, (b) helium ions, and (c) oxygen ions to ambient electrons due to Coulomb collision. The heat flux from Coulomb collision were calculated from the ion flux observed by Arase/MEP-i and the electron density based on the UHR frequency observed by Arase/PWE based on the methods of Fok et al. (1991) and Jordanova et al. (1996). The minimum and maximum energies for the calculation were 5.0 and 109 keV/q, respectively. The composition of the plasmaspheric plasma was assumed to be H^+:He^+:O^+ = 77:20:3, and the temperature of plasmaspheric plasma was assumed to be 1 eV. Figure 9d shows the total heat flux due to Coulomb collisions with these ions. Note that these heat fluxes are the sums of those flowing into both hemispheres. Thus, we should divide the rates by two to estimate the amount for one hemisphere. The heat flux reaching each hemisphere may not be the same (Mendillo & Wroten, 2019). Figure 9e indicates the 630.0 nm airglow/auroral intensity observed at the Arase footprint and is based on the same data as are Figures 6f, 7e, and 8g. The estimated heat flux due to Coulomb collisions between electrons and oxygen ions (>~5 keV/q) is on the order of 10^7 eV/cm^2/s. According to Kozyra et al. (1993), the generation of SAR arcs requires a heat flux on the order of 10^9–10^{10} eV/cm^2/s, indicating that the estimated heat flux due to Coulomb collisions between electrons and oxygen ions (>~5 keV/q) is too small to contribute to the generation of the SAR arc. This result suggests that the local enhancement of oxygen ions observed by MEP-i is not essential for the generation of the SAR arc.

We next discuss the latter possibility that the ring-current ions below ~5 keV/q mainly contribute to the thin structure of the SAR arc. As can be seen from Figure 9d, the total heat flux does not reach the order of 10^9–10^{10} eV/cm^2/s. The reason for this is possibly that the heat flux from Coulomb collision was underestimated because ion fluxes with an energy of 5 keV/q or higher measured by Arase/MEP-i were used; unfortunately, LEP-i (Asamura et al., 2018) data covering lower energies were not available during this event. According to Kozyra et al. (1993), the most efficient particles of energy transfer to plasmaspheric electrons are protons with energies of ~1–2 keV, helium ions with energies of ~7 keV, and oxygen ions with energies of ~ 30 keV. Coulomb collisions with protons and helium ions below 5 keV/q were not included in the present calculations, which may have led to the underestimation of the heat flux. The low-energy ions at energies below 5.0 keV/q, which could not be observed at this time, may contribute to the generation of the SAR arc via Coulomb collision. Ions with energies ranging from ~1 keV to a few hundreds keV contribute to the storm-time ring-current (Smith & Hoffman, 1973). Additionally, the empirical model of low-energy ring-current ions constructed by Collin et al. (1993) shows that the average proton flux at energies below 1 keV is ~10^6/s-cm^2-sr-keV/q at L = 3.5–4.5. These facts indicate that low-energy protons below 5.0 keV/q may be important for the generation of SAR arcs. The oxygen torus, which is an enhanced low-energy oxygen-ion mass near the plasmapause (e.g., Fraser et al., 2005; Nosé et al., 2015), may also has

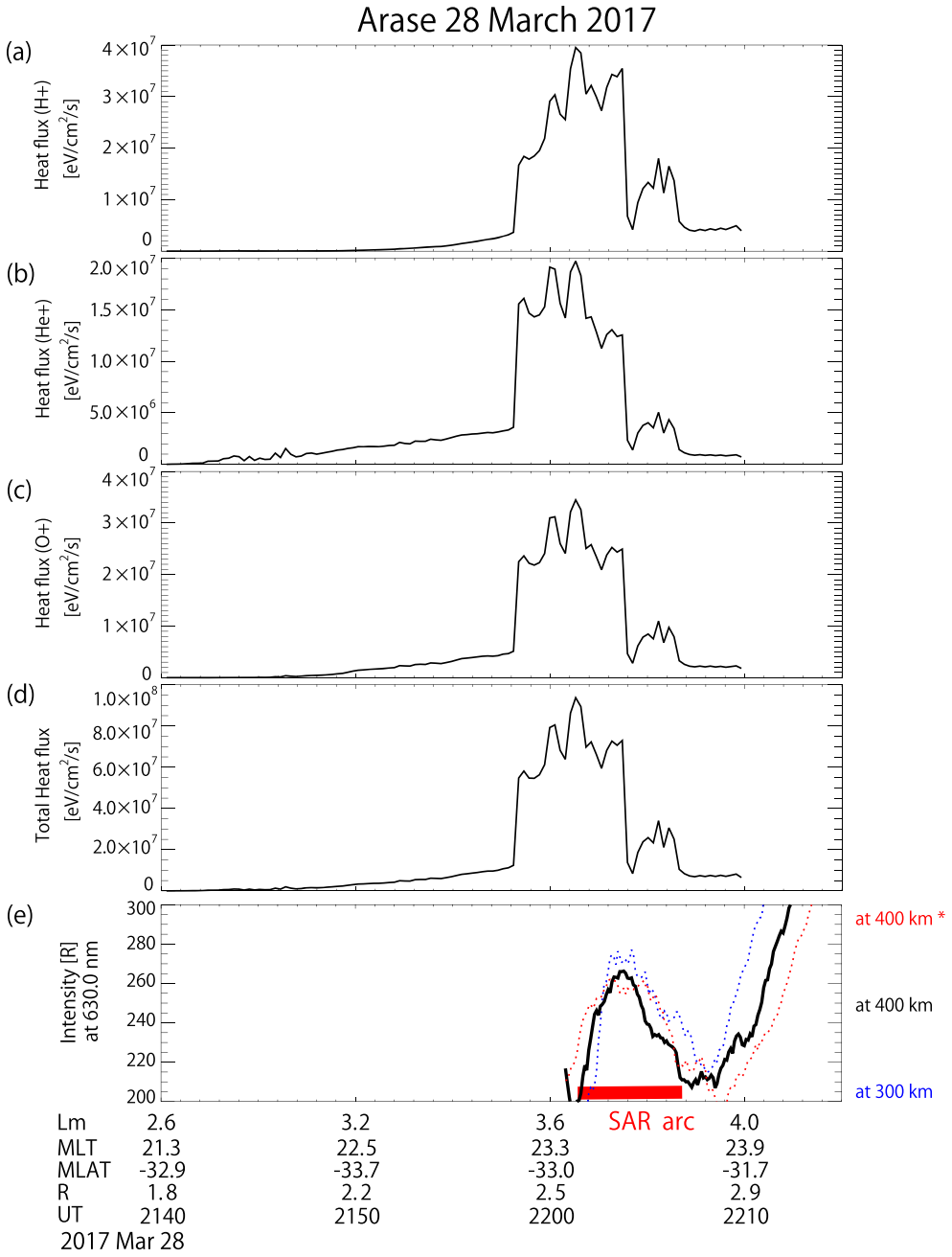

Figure 9. Calculated heat flux due to Coulomb collision between electrons and (a) protons, (b) helium ions, and (c) oxygen ions. The heat fluxes were obtained from MEP-i and electron density (estimated from UHR frequency) observed by Arase. The composition of the plasmaspheric plasma was assumed to be H^+:He^+:O^+ = 77:20:3 and the temperature was assumed to be 1 eV. (d) Total heat flux. (e) 630.0 nm airglow/auroral intensity observed at Nyrölä at the Arase footprint. Panel (e) is based on the same data as Figures 6f, 7e, and 8g.

some association with the SAR arc generation. In the future, these possibilities should be investigated by studying more conjunction events using LEP-i.

The reason why the SAR arc investigated in this study is latitudinally thin may also be related to the ionospheric trough. As shown in Figure 4, the location of the minimum of this trough almost coincides with the location of the SAR arc over the time during which it occurs. The Swarm-A and -C data presented in Figure 5 show high electron temperature and a localized small enhancement of electron density in the trough minimum at the SAR arc crossing. These facts indicate that the heated electrons in the plasma

plume excite 630 nm emission only at the location near the trough minimum. Past studies suggested that the ionospheric electron density is important for the generation of SAR arcs because the cooling of the electrons by the ions in the ionosphere is less efficient in the trough region (e.g., Kozyra et al., 1990; Kozyra & Nagy, 1997; Rees & Roble, 1975). The heated electrons are cooled through collision with ambient ions in the ionosphere (e.g., Su et al., 2015), while the heated electrons in the trough region lose less heat due to the lower ion density. Moreover, ionospheric electrons in the trough region can absorb a larger share of heat from the magnetospheric heat flux due to its low density, causing localized enhancement of electron temperature (e.g., Prolss, 2006). For these reasons, 630 nm emission may be confined around the trough minimum. However, the bright SAR arc at the moment of detachment is located at slightly higher latitudes than the trough minimum, as shown in Figure 4b. This may be related to the fact that the SAR arc appears on the poleward side of the trough immediately after its generation, where there is a larger amount of ionospheric electrons compared with the trough minimum, leading to a brighter emission. These observation results show the importance of the mutual relationship between the position of the heat flux supplied from the magnetosphere and the position of the ionospheric trough.

4.2. EMIC Waves and KAWs as a Source of SAR-Arc Energy

As can be seen from the spectra in Figures 8a–8c, the enhanced EMIC waves are not visible above the SAR arc as compared with the non-SAR arc region. Anderson et al. (1992a, 1992b) showed the average PSDs of EMIC waves is ~5.0 nT^2/Hz, while Yuan et al. (2014) showed using data from the Cluster satellite that cold electrons in a plasma plume were heated by Landau damping of EMIC waves with PSDs of 10–100 nT^2/Hz. However, the PSDs shown in Figure 8 are mostly less than 10^{-2} nT^2/Hz, and clear EMIC waves are not observed. The PSD enhancements at both ends and peak intensity of the SAR arc are also too weak to generate SAR arc and do not correspond to the structure of the SAR arc. Thus, we conclude that the EMIC waves in this frequency range did not contribute to the emission of the detached SAR arc observed in the present study. It should be noted that Arase was located at slightly high latitudes (MLAT: ~−32°N) at the time that it crossed the SAR arc. EMIC waves could be confined near the equatorial plane of the magnetosphere and thus might not have been observed at the off-equatorial location. Lotoaniu et al. (2005) concluded that the source region of EMIC waves was within 11°|MLAT|. However, statistical analysis by Allen et al. (2015) and an event study by Yuan et al. (2014) suggested that EMIC waves can be observed even at latitudes above 30°|MLAT|.

We also verified the possibility that KAWs heat plasmaspheric electrons. There are a few limited observations of KAWs in the literature. For example, using data from the Cluster satellite, Chaston et al. (2005) reported the observation of KAWs with PSDs of about 10^5–10^6 nT^2/Hz at a frequency of ~10 mHz. Additionally, Lanzerotti et al. (1978) reported the observation of KAWs at frequencies of ~8.3 and ~9.5 mHz using ground-based measurements in a conjugate region of SAR arcs. Based on these past observations, we evaluate the magnetic field variation around ~10 mHz as shown in Figures 8d–8f. As seen in these panels, local enhancement of PSDs associated with the SAR arc was not observed. The PSDs at ~10 mHz above the SAR arc were at most ~5 nT^2/Hz. Past studies concluded that a magnetic field amplitude of ~10 nT might be able to produce a SAR arc, although large uncertainties existed (e.g., Hasegawa & Mima, 1978; Lanzerotti et al., 1978; Kozyra & Nagy, 1997). If there is a wave with a magnetic field amplitude of ~10 nT and a frequency of 10 mHz, the PSDs will be ~1.0×10^4 nT^2/Hz. However, the PSDs of the waves observed by Arase over the SAR arc at a frequency of ~10 mHz do not even reach the order of 10 nT^2/Hz. The magnetic field deviation from 5 min running averages shown in Figure 7d also supports the absence of magnetic waves with an amplitude of 10 nT. These results strongly suggest that KAWs were not associated with the present SAR arc. Previous simulations have predicted that KAWs will be generated near the magnetic equator (Lysak & Carlson, 1981). During the event analyzed in the present study, Arase was located at an MLAT of ~−32°N. However, it is not likely that the KAWs which were three orders of magnitude stronger than that observed by Arase were confined to the equatorial plane at MLATs of less than 32°.

5. Conclusions

This study reports observations of the conjunction event of a SAR arc from the Arase satellite on 28 March 2017. The event has provided us with an opportunity to conduct quantitative evaluation of the SAR-arc generation mechanism based on the in-situ observation in the magnetosphere, which has not been done previously. The results of the present analysis are summarized as follows:

1. Observations from Swarm-A and -C showed that electron density decreased and the electron temperature increased above the SAR arc. Additionally, the electron density slightly increased at the location of the SAR arc. This may indicate the supply (precipitation) of electrons to the SAR arc from the magnetosphere due to electron heating by Coulomb collisions. Swarm satellites did not observe clear field-aligned currents above the SAR arc.
2. The location of the minimum of the ionospheric trough almost coincides with the location of the SAR arc in Figure 4. This latitudinally narrow low-density trough minimum creates preferable conditions for 630.0 nm emission at the SAR arc. In low-density plasma, electrons lose less energy in collisions with ambient ions and can absorb a larger heat share from the magnetospheric heat flux. However, the bright SAR arc at the moment of detachment is located at latitudes slightly higher than the trough minimum.
3. Ring-current ion fluxes and electron densities observed by Arase suggest that the source of the observed SAR arc was located in the overlap region of the plasmaspheric plume and the ring-current ions. The peak intensity of the SAR arc takes place at the poleward edge of the plasmaspheric plume.
4. We evaluated the heat flux from Coulomb collisions between plasmaspheric plasma and ring-current ions based on the Arase observations. From the evaluation, we conclude that the observed enhancement of oxygen ions of 8–20 keV/q was not the main source of the SAR arc. Because the heat flux is expected to increase at lower ion energies, we infer that low-energy ions (especially protons at energies below 5.0 keV/q), which were not observed in the present study due to a lack of LEP-i observation, efficiently transport the energy that generates SAR arcs via Coulomb collision.
5. The observed electromagnetic waves were too weak to have caused the SAR arc. We conclude that the EMIC waves (0.3–10 Hz) and KAWs (1–62.5 mHz) did not contribute to the emission of the SAR arc observed in the present study.

From these results, we conduct first quantitative evaluation of the possible SAR-mechanisms and conclude that the plasmaspheric electrons were heated by Coulomb collision and their moderate precipitation to the ionosphere generated the SAR arc. However, the mechanism that determines the latitudinal width of the observed SAR arc has not been fully clarified, since the overlap between any combinations of the observed plasmaspheric plume, ring-current ions, and ionospheric trough has a greater latitudinal width than the observed SAR arc. For the present event, we could not investigate low-energy ion features due to a lack of LEP-i data. The present study shows the more conjunction events of SAR arcs with Arase and/or Van Allen Probes can clarify the above open questions.

Data Availability Statement

Swarm data were provided by ESA and are available online (https://earth.esa.int/web/guest/swarm/data-access). The SYM-H, AU, and AL indices were provided by World Data Center (WDC) for Geomagnetism at Kyoto University, Japan. Scientific data of the ERG (Arase) satellite were obtained from the ERG Science Center (ERG-SC) operated by ISAS/JAXA and ISEE/Nagoya University (https://ergsc.isee.nagoya-u.ac.jp/index.shtml.en, Miyoshi, Hori, et al., 2018). The present study analyzed LEP-e-L2 v02_02 data, MEP-i-L2 v02_00 data, PWE/EFD/E_spin-L2 v03_01 data, PWE/EFD/pot-L2 v03_01 data, PWE/HFA-L2 v01_01 and MGF-L2 v03_04 data, MGF/64 Hz-L2 v03_03 data, and L2 v02 orbit data. The optical data from Nyrölä are available from the ISEE through the ERG-SC. The PWING observation data and geomagnetic indices (AE and SYM-H) are distributed by the Inter-university Upper atmosphere Global Observation Network (IUGONET) project of the Ministry of Education, Culture, Sports, Science and Technology of Japan. The OMNI data were provided by the GSFC/SPDF OMNIWeb interface (http://omniweb.gsfc.nasa.gov). The solar wind parameters and W-parameters for driving TS05 model were provided by TS05 web repository (http://geo.phys.spbu.ru/~tsyganenko/TS05_data_and_stuff/). The GNSS-TEC data providers are listed at http://stdb2.isee.nagoya-u.ac.jp/GPS/GPS-TEC/gnss_provider_list.html.

Acknowledgments

We thank Y. Katoh, H. Hamaguchi, Y. Yamamoto, and T. Adachi of ISEE, Nagoya University and Astronomical Association Jyväskylän Sirius, Jyväskylä, Finland, for their continuous support in the observations at Nyrölä, Finland. This work was supported by Grants-in-Aid for Scientific Research (15H05815, 15H05747, 16H06286, 17H00728, and 20H01959) and by Birateral Program (JPJSBP120194814) from the Japan Society for the Promotion of Science. Part of the work of YM, TH, and MS was performed at ERG-SC.

References

Allen, R. C., Zhang, J.-C., Kistler, L. M., Spence, H. E., Lin, R.-L., Klecker, B., et al. (2015). A statistical study of EMIC waves observed by cluster: 1. Wave properties. *Journal of Geophysical Research: Space Physics*, *120*, 5574–5592.

Anderson, B. J., Erlandson, R. E., & Zanetti, L. J. (1992a). A statistical study of Pc 1–2 magnetic pulsations in the equatorial magnetosphere:1. Equatorial occurrence distributions. *Journal of Geophysical Research*, *97*, 3075–3088. https://doi.org/10.1029/91JA02706

Anderson, B. J., Erlandson, R. E., & Zanetti, L. J. (1992b). A statistical study of Pc 1–2 magnetic pulsations in the equatorial magnetosphere:2. Wave properties. *Journal of Geophysical Research*, *97*(A3), 3089–3101. https://doi.org/10.1029/91JA02697

Anderson, P. C., Hanson, W. B., Coley, W. R., & Hoegy, W. R. (1994). *Journal Geophysics Research*, *99*, 3985. https://doi.org/10.1029/93JA02104

Angelopoulos, V., Cruce, P., Drozdov, A., Grimes, E. W., Hatzigeorgiu, N., King, D. A., et al. (2019). The space physics environment data analysis system (SPEDAS). *Space Science Reviews*, *215*, 9. https://doi.org/10.1007/s11214-018-0576-4

Asamura, K., Kazama, Y., Yokota, S., Kasahara, S., & Miyoshi, Y. (2018). Low-energy particle experiments-ion mass analyzer (LEPi) onboard the ERG (Arase) satellite. *Earth, Planets and Space*, *70*(1), 70. https://doi.org/10.1186/s40623-018-0846-0

Barbier, D. (1958). The auroral activity at low latitudes. *Annals of Geophysics*, *1*, 4334–4355.

Burke, W. J., Gussenhoven, M. S., Kelley, M. C., Hardy, D. A., & Rich, F. J. (1982). Electric and magnetic field characteristics of discrete arcs in the polar cap. *Journal of Geophysical Research*, *87*, 2431–2443. https://doi.org/10.1029/JA087iA04p02431

Chaston, C. C., Peticolas, L. M., Carlson, C. W., McFadden, J. P., Mozer, F., Wilber, M., et al. (2005). Energy deposition by Alfvén waves into the dayside auroral oval: Cluster and FAST observations. *Journal of Geophysical Research*, *110*, A02211. https://doi.org/10.1029/2004JA010483

Chen, L., Thorne, R. M., & Horne, R. H. (2009). Simulation of EMIC excitation in a model magnetosphere including structured high-density plumes. *Journal of Geophysical Research*, *114*, A07221. https://doi.org/10.1029/2009JA014204

Chu, X., Malaspina, D., Gallardo-Lacourt, B., Liang, J., Andersson, L., Ma, Q., et al. (2019). Identifying STEVE's magnetospheric driver using conjugate observations in the magnetosphere and on the ground. *Geophysical Research Letters*, *46*, 12,665–12,674. https://doi.org/10.1029/2019GL082789

Cole, K. (1965). Stable auroral red arcs, sinks for energy of Dst main phase. *Journal of Geophysical Research*, *70*, 1689–1706. https://doi.org/10.1029/JZ070i007p01689

Collin, H. L., Quinn, J. M., & Cladis, J. B. (1993). An empirical static model of low energy ring-current ions. *Geophysical Research Letters*, *20*(2), 141–144. https://doi.org/10.1029/93GL00066

Cornwall, J. M., Coroniti, F. V., & Thorne, R. M. (1971). Unified theory of SAR arc formation at the plasmapause. *Journal of Geophysical Research*, *76*, 4428–4445. https://doi.org/10.1029/JA076i019p04428

Coroniti, F. V., & Pritchett, P. L. (2014). The quiet evening auroral arc and the structure of the growth phase near-Earth plasma sheet. *Journal of Geophysical Research: Space Physics*, *119*, 1827–1836. https://doi.org/10.1002/2013JA019435

de Soria-Santacruz, M., Spasojevic, M., & Chen, L. (2013). EMIC waves growth and guiding in the presence of cold plasma density irregularities. *Geophysical Research Letters*, *40*, 1940–1944. https://doi.org/10.1002/grl.50484

Ejiri, M. (1978). Trajectory traces of charged particles in the magnetosphere. *Journal of Geophysical Research*, *83*, 4798–4810. https://doi.org/10.1029/JA083iA10p04798

Fok, M.-C., Kozyra, J. U., Nagy, A. F., & Cravens, T. E. (1991). Lifetime of ring current particles due to Coulomb collisions in the plasmasphere. *Journal of Geophysical Research*, *96*(A5), 7861–7867. https://doi.org/10.1029/90JA02620

Foster, J. C., Buonsanto, M. J., Mendillo, M., Nottingham, D., Rich, F. J., & Denig, W. (1994). Coordinated stable auroral red arc observations: Relationship to plasma convection. *Journal of Geophysical Research*, *99*, 11,429–11,439. https://doi.org/10.1029/93JA03140

Fraser, B. J., Horwitz, J. L., Slavin, J. A., Dent, Z. C., & Mann, I. R. (2005). Heavy ion mass loading of the geomagnetic field near the plasmapause and ULF wave implications. *Geophysical Research Letters*, *32*, L04102. https://doi.org/10.1029/2004GL021315

Hasegawa, A., & Mima, K. (1978). Anomalous transport produced by kinetic Alfven wave turbulence. *Journal of Geophysical Research*, *83*, 1117–1123. https://doi.org/10.1029/JA083iA03p01117

Horwitz, J. L., Comfort, R. H., Brace, L. H., & Chappell, C. R. (1986). Dual-spacecraft measurements of plasmasphere-ionosphere coupling. *Journal of Geophysical Research*, *91*(A10), 11,203–11,216. https://doi.org/10.1029/JA091iA10p11203

Iyemori, T. (1990). Storm-time magnetospheric currents inferred from mid-latitude geomagnetic field variations. *Journal of Geomagnetism and Geoelectricity*, *42*(11), 1249–1265. https://doi.org/10.5636/jgg.42.1249

Iyemori, T., & Rao, D. R. K. (1996). Decay of the Dst field of geomagnetic disturbance after substorm onset and its implication to storm-substorm relation. *Annales de Geophysique*, *14*(6), 608–618. https://doi.org/10.1007/s00585-996-0608-3

Jordanova, V. K., Kistler, L. M., Kozyra, J. U., Khazanov, G. V., & Nagy, A. F. (1996). Collisional losses of ring-current ions. *Journal of Geophysical Research*, *101*(A1), 111–126. https://doi.org/10.1029/95JA02000

Kasaba, Y., Ishisaka, K., Kasahara, Y., Imachi, T., Yagitani, S., Kojima, H., et al. (2017). Wire probe antenna (WPT) and electric field detector (EFD) of plasma wave experiment (PWE) aboard the Arase satellite: Specifications and initial evaluation results. *Earth, Planets and Space*, *69*, 174. https://doi.org/10.1186/s40623-017-0760-x

Kasahara, Y., Kasaba, Y., Kojima, H., Yagitani, S., Ishisaka, K., Kumamoto, A., et al. (2018). The plasma wave experiment (PWE) onboard the Arase (ERG) satellite. *Earth, Planets and Space*, *70*(1), 86. https://doi.org/10.1186/s40623-018-0842-4

Kazama, Y., Wang, B. J., Wang, S. Y., Ho, P. T. P., Tam, S. W. Y., Chang, T. F., et al. (2017). Low-energy particle experiments-electron analyzer (LEPe) onboard the Arase spacecraft. *Earth, Planets and Space*, *69*, 165. https://doi.org/10.1186/s40623-017-0748-6

Knudsen, D. J., Burchill, J. K., Buchert, S. C., Eriksson, A. I., Gill, R., Wahlund, J.-E., et al. (2017). Thermal ion imagers and Langmuir probes in the swarm electric field instruments. *Journal of Geophysics Research: Space Physics*, *122*, 2655–2673. https://doi.org/10.1002/2016JA022571

Kozyra, J. U., Chandler, M. O., Hamilton, D. C., Peterson, W. K., Klumpar, D. M., Slater, D. W., et al. (1993). The role of ring current nose events in producing stable auroral red arc intensifications during the main phase: Observations during the September 19-24, 1984 equinox transition study. *Journal of Geophysical Research*, *98*, 9267. https://doi.org/10.1029/92JA02554

Kozyra, J. U., & Nagy, A. F. (1997). High-altitude energy source(s) for stable auroral red arcs. *Reviews of Geophysics*, *35*, 155, 96RG03194–190.

Kozyra, J. U., Shelley, E. G., Comfort, R. H., Brace, L. H., Cravens, T. E., & Nagy, A. F. (1987). The role of ring current O^+ in the formation of stable auroral red arcs. *Journal of Geophysical Research*, *92*, 7487–7502. https://doi.org/10.1029/JA092iA07p07487

Kozyra, J. U., Valladares, C. E., Carlson, H. C., Buonsanto, M. J., & Slater, D. W. (1990). A theoretical study of the seasonal and solar cycle variations of stable auroral red arcs. *Journal of Geophysical Research*, *95*, 12219. https://doi.org/10.1029/JA095iA08p12219

Kumamoto, A., Tsuchiya, F., Kasahara, Y., Kasaba, Y., Kojima, H., Yagitani, S., et al. (2018). High frequency analyzer (HFA) of plasma wave experiment (PWE) onboard the Arase spacecraft. *Earth, Planets and Space*, *70*(1), 82. https://doi.org/10.1186/s40623-018-0854-0

Lanzerotti, L. J., Hasagawa, A., & Maclennan, C. G. (1978). Hydromagnetic waves as a cause of a SAR arc event. *Planetary and Space Science*, *26*, 777–783. https://doi.org/10.1016/0032-0633(78)90008-9

Lomidze, L., Knudsen, D. J., Burchill, J., Kouznetsov, A., & Buchert, S. C. (2018). Calibration and validation of swarm plasma densities and electron temperatures using ground-based radars and satellite radio occultation measurements. *Radio Science*, *53*, 15–36. https://doi.org/10.1002/2017RS006415

Lotoaniu, T. M., Fraser, B. J., & Waters, C. L. (2005). Propagation of electromagnetic ion cyclotron wave energy in the magnetosphere. *Journal of Geophysical Research*, *110*, A07214. https://doi.org/10.1029/2004JA010816

Lysak, R. L., & Carlson, C. W. (1981). The effect of microscopic turbulence on magnetosphere-ionosphere coupling. *Geophysical Research Letters*, *8*, 269–272. https://doi.org/10.1029/GL008i003p00269

Marovich, E. (1966). Fritz peak observations of stable auroral red arcs, summary 1955-1965, *Tech. Rep*., IER 16-1TSA 16, 68 pp., NOAA, Boulder, Colo.

Martinis, C., Baumgardner, J., Mendillo, M., Taylor, M. J., Moffat-Griffin, T., Wroten, J., et al. (2019). First ground-based conjugate observations of stable auroral red (SAR) arcs. *Journal of Geophysical Research: Space Physics*, *124*, 4658–4671. https://doi.org/10.1029/2018JA026017

Matsuoka, A., Teramoto, M., Nomura, R., Nosé, M., Fujimoto, A., Tanaka, Y., et al. (2018). The ARASE (ERG) magnetic field investigation. *Earth, Planets and Space*, *70*(1). https://doi.org/10.1186/s40623-018-0800-1

McIlwain, C. E. (1961). Coordinates for mapping the distribution of magnetically trapped particles. *Journal of Geophysical Research*, *66*(11), 3681–3691. https://doi.org/10.1029/JZ066i011p03681

Mendillo, M., Baumgardner, J., & Wroten, J. (2016). SAR arcs we have seen: Evidence for variability in stable auroral red arcs. *Journal of Geophysical Research: Space Physics*, *121*, 245–262. https://doi.org/10.1002/2015JA021722

Mendillo, M., Baumgardner, J., Wroten, J., Martinis, C., Smith, S., Merenda, K.-D., et al. (2013). Imaging magnetospheric boundaries at ionospheric heights. *Journal of Geophysical Research: Space Physics*, *118*, 7294–7305. https://doi.org/10.1002/2013JA019267

Mendillo, M., & Wroten, J. (2019). Modeling stable auroral red (SAR) arcs at geomagnetic conjugate points: Implications for hemispheric asymmetries in heat fluxes. *Journal of Geophysical Research: Space Physics*, *124*, 6330–6342. https://doi.org/10.1029/2019JA026904

Miyoshi, Y., Hori, T., Shoji, M., Teramoto, M., Chang, T. F., Matsuda, S., et al. (2018). The ERG science center. *Earth, Planets and Space*, *70*(1), 96. https://doi.org/10.1186/s40623-018-0867-8

Miyoshi, Y., Shinohara, I., Takashima, T., Asamura, K., Higashio, N., Mitani, T., et al. (2018). Geospace exploration project ERG. *Earth, Planets and Space*, *70*(1). https://doi.org/10.1186/s40623-018-0862-0,101

Nosé, M., Oimatsu, S., Keika, K., Kletzing, C. A., Kurth, W. S., Pascuale, S. D., et al. (2015). Formation of the oxygen torus in the inner magnetosphere: Van Allen probes observations. *Journal of Geophysical Research: Space Physics*, *120*, 1182–1196. https://doi.org/10.1002/2014JA020593

Olsen, N., Stolle, C., Floberghagen, R., Hulot, G., & Kuvshinov, A. (2016). Special issue "swarm science results after 2 years in space". *Earth, Planets and Space*, *68*, 172. https://doi.org/10.1186/s40623-016-0546-6

Otsuka, Y., Ogawa, T., Saito, A., Tsugawa, T., Fukao, S., & Miyazaki, S. (2002). A new technique for mapping of total electron content using GPS network in Japan. *Earth, Planets and Space*, *54*(1), 63–70. https://doi.org/10.1186/BF03352422

Prolss, G. W. (2006). Subauroral electron temperature enhancement in the nighttime ionosphere. *Annales de Geophysique*, *24*, 1871–1885. https://doi.org/10.5194/angeo-24-1871-2006

Rees, M. H., & Roble, R. G. (1975). Observations and theory of the formation of stable auroral red arcs. *Reviews of Geophysics and Space Physics*, *13*, 201–242. https://doi.org/10.1029/RG013i001p00201

Roach, F. E., & Roach, J. R. (1963). Stable 6300Å auroral arcs in midlatitudes. *Planetary and Space Science*, *I1*, 523–545.

Shiokawa, K., Hosokawa, K., Sakaguchi, K., Ieda, A., Otsuka, Y., Ogawa, T., & Connors, M. (2009). The optical mesosphere thermosphere imagers (OMTIs) for network measurements of aurora and airglow, future perspectives of space plasma and particle instrumentation and international collaborations. *AIP Conference Proceedings, 1144*, 212–215. https://doi.org/10.1063/1.3169292

Shiokawa, K., Katoh, Y., Hamaguchi, Y., Yamamoto, Y., Adachi, T., Ozaki, M., et al. (2017). Ground-based instruments of the PWING project to investigate dynamics of the inner magnetosphere at subauroral latitudes as a part of the ERG-ground coordinated observation network. *Earth, Planets and Space*, *69*(1), 160. https://doi.org/10.1186/s40623-017-0745-9

Shiokawa, K., Katoh, Y., Satoh, M., Ejiri, M. K., & Ogawa, T. (2000). Integrating-sphere calibration of all-sky cameras for nightglow measurements. *Advances in Space Research*, *26*, 1025–1028. https://doi.org/10.1016/S0273-1177(00)00052-1

Shiokawa, K., Katoh, Y., Satoh, M., Ejiri, M. K., Ogawa, T., Nakamura, T., et al. (1999). Development of optical mesosphere thermosphere imagers (OMTI). *Earth, Planets and Space*, *51*, 887–896. https://doi.org/10.1186/BF03353247

Shiokawa, K., Miyoshi, Y., Brandt, P. C., Evans, D. S., Frey, H. U., Goldstein, J., & Yumoto, K. (2013). Ground and satellite observations of low-latitude red auroras at the initial phase of magnetic storms. *Journal of Geophysical Research: Space Physics*, *118*, 256–270. https://doi.org/10.1029/2012JA018001

Shiokawa, K., Yumoto, K., Nishitani, N., Hayashi, K., Oguti, T., McEwen, D. J., et al. (1996). Quasi-periodic poleward motions of sun-aligned auroral arcs in the high-latitude morning sector: A case study. *Journal of Geophysical Research*, *101*, 19,789–19,800. https://doi.org/10.1029/96JA01202

Smith, P. H., & Hoffman, R. A. (1973). Ring current particle distributions during the magnetic storms of December 16–18, 1971. *Journal of Geophysical Research*, *78*(22), 4731–4737. https://doi.org/10.1029/JA078i022p04731

Smith, P. H., & Hoffman, R. A. (1974). Direct observations in the dusk hours of the characteristics of the storm time ring current particles during the beginning of magnetic storms. *Journal of Geophysical Research*, *79*, 966–971. https://doi.org/10.1029/JA079i007p00966

Su, F., Wang, W., Burns, A. G., Yue, X., & Zhu, F. (2015). The correlation between electron temperature and density in the topside ionosphere during 2006–2009. *Journal of Geophysical Research: Space Physics*, *120*, 10,724–10,739. https://doi.org/10.1002/2015JA021303

Takagi, Y., Shiokawa, K., Otsuka, Y., Connors, M., & Schofield, I. (2018). Statistical analysis of SAR arc detachment from the main oval based on 11-year, all-sky imaging observation at Athabasca, Canada. *Geophysical Research Letters*, *45*, 11,539–11,546. https://doi.org/10.1029/2018GL079615

Thébault, E., Finlay, C. C., Beggan, C. D., Alken, P., Aubert, J., Barrois, O., et al. (2015). International geomagnetic reference field: The 12th generation. *Earth, Planets and Space*, *67*, 79. https://doi.org/10.1186/s40623-015-0228-9

Tsyganenko, N. A. (2002a). A model of the near magnetosphere with a dawn-dusk asymmetry 1. Mathematical structure. *Journal of Geophysical Research*, *107*, 1–17.

Tsyganenko, N. A. (2002b). A model of the near magnetosphere with a dawn-dusk asymmetry 2. Parameterization and fitting to observations. *Journal of Geophysical Research*, *107*, 1–17.

Tsyganenko, N. A., & Sitnov, M. I. (2005). Modeling the dynamics of the inner magnetosphere during strong geomagnetic storms. *Journal of Geophysical Research*, *110*(A3), 1–16. https://doi.org/10.1029/2004JA010798

Vallat, C., Ganushkina, N., Dandouras, I., Escoubet, C. P., Taylor, M. G. G. T., Laakso, H., et al. (2007). Ion multi-nose structures observed by cluster in the inner magnetosphere. *Annales de Geophysique*, *25*, 171–190. https://doi.org/10.5194/angeo-25-171-2007

Wang, B., Li, P., Huang, J., & Zhang, B. (2019). Nonlinear Landau resonance between EMIC waves and cold electrons in the inner magnetosphere. *Physics of Plasmas*, *26*, 042903. https://doi.org/10.1063/1.5088374

World Data Center for Geomagnetism, Kyoto, Nose, M., Iyemori, T., Sugiura, M., & Kamei, T. (2015). Geomagnetic AE index, https://doi.org/10.17593/15031-54800

Yokota, S., Kasahara, S., Mitani, T., Asamura, K., Hirahara, M., Takashima, T., et al. (2017). Medium-energy particle experiments-ion mass analyzer (MEP-i) onboard ERG (Arase). *Earth, Planets and Space*, *69*, 172. https://doi.org/10.1186/s40623-017-0754-8

Yuan, Z., Xiong, Y., Huang, S., Deng, X., Pang, Y., Zhou, M., et al. (2014). Cold electron heating by EMIC waves in the plasmaspheric plume with observations of the cluster satellite. *Geophysical Research Letters*, *41*, 1830–1837. https://doi.org/10.1002/2014GL059241